High-frequency response of wind-driven currents measured by drifting buoys and altimetry over the world ocean

M.-H. Rio[1] and F. Hernandez

CLS, Space Oceanography Division, Ramonville, France

Received 26 September 2002; revised 20 February 2003; accepted 9 April 2003; published 29 August 2003.

[1] We investigate the wind-driven current response over the world ocean using SVP drifting buoys, ERS-1 and ERS-2, and TOPEX altimetry data and ECMWF wind stress fields. Wind-driven ageostrophic currents are estimated from drifting buoys by removing altimetry deduced geostrophic currents from observed drifting velocities. Removing the geostrophic signal enhances the coherence with wind stress at periods longer than 10 days. For superinertial periods lower than 20 days, a two-parameter (i.e., angle and amplitude) model is fitted to the isolated ageostrophic signal to study the upper ocean response to surface wind stress in that frequency band. The model, which can explain up to 30% of the variance in some areas, indicates that the currents spiral to the right (left) of the wind with depth in the Northern (Southern) Hemisphere, in agreement with the Ekman theory. The absolute value of the angle parameter is found to exhibit significant spatial and seasonal variability. The vertical eddy viscosity and the Ekman layer depth as deduced from Ekman theory are compared to previous results. Their seasonal variability is also studied. Model results are then used to compute the mean and standard deviation of ageostrophic currents in 5° boxes over the world ocean. The equatorial divergence and the subpolar and subtropical convergence zones are well reproduced. *INDEX TERMS:* 4508 Oceanography: Physical: Coriolis effects; 4512 Oceanography: Physical: Currents; 4572 Oceanography: Physical: Upper ocean processes; *KEYWORDS:* altimetry, drifting buoys, Ekman current's modeling, rotary spectra, Ekman depth, eddy viscosity

Citation: Rio, M.-H., and F. Hernandez, High-frequency response of wind-driven currents measured by drifting buoys and altimetry over the world ocean, *J. Geophys. Res.*, *108*(C8), 3283, doi:10.1029/2002JC001655, 2003.

1. Introduction

[2] Wind-driven currents were theoretically described by Ekman at the beginning of the twentieth century [*Ekman*, 1905], but they remain difficult to observe in the open ocean. Our goal is to investigate and observe the Ekman-like response of subsurface currents to wind stress for periods ranging between the inertial period and a few days on a global scale. The study is based on two steps: (1) extraction of only wind-driven currents from the velocities measured by drifting buoys and (2) parameterization of the subsurface current response to wind stress using a wind-driven current model.

[3] Extracting the wind-driven flow contribution from the total observed flow is a challenge. Other than wind-driven contributions, internal waves and free inertial motions occur at high frequencies, while at subinertial frequencies, geostrophic currents dominate [*Rudnick and Weller*, 1993]. Below the mixed layer, part of the geostrophic currents can be indirectly due to local (or nonlocal) wind forcing through pressure gradient (i.e., Ekman pumping) and can therefore be wind coherent [*Weller et al.*, 1991; *Lee*, 1996].

[4] Various approaches exist to extract the local wind-driven flow from the total oceanographic signal as measured by drifting buoys, current meters, or Acoustic Doppler Current Profilers (ADCP). Many authors [*Davis et al.*, 1981; *Price et al.*, 1987; *Weller et al.*, 1991; *Schudlich and Price*, 1998] have considered that the wind-driven flow was trapped within the mixed layer and extracted it from the observed flow by removing the geostrophic flow component estimated at the base of the mixed layer (i.e., a reference geostrophic current). The limitation of this method is that results vary with the chosen reference depth. A different method is used by *Chereskin and Roemmich* [1991] at 11°N in the Atlantic Ocean and *Wijffels et al.* [1994] at 10°N in the Pacific. They consider simultaneous measurements of hydrographic and ADCP data and compute the ageostrophic, wind-driven shear as the difference between total shear observed by the ADCP and geostrophic shear derived from hydrographic observations. In the Atlantic Subtropical Convergence Zone, *Lee* [1996] deduced geostrophic currents from horizontal pressure gradients calculated using density measurements from a horizontal array of instruments. Geostrophic currents can also be estimated from climatologies as shown by *Ralph and Niiler* [1999].

[1]Now at Istituto di Scienze dell'Atmosfera e del Clima-CNR, Rome, Italy.

0148-0227/03/2002JC001655$09.00

A recent approach is to compute geostrophic currents from satellite altimetry. *Lagerloef et al.* [1999] used altimetry and wind stress data to estimate the geostrophic and Ekman components from surface drifter velocities in the tropical Pacific using a complex multiple linear regression.

[5] In the present study, geostrophic velocities are computed from satellite altimetry and are subtracted from surface currents as given by drifter trajectories to estimate ageostrophic currents. However, removing geostrophic currents is not enough to isolate wind-driven flow. Unwanted remaining contributions are residual mesoscale variability (not well resolved by altimetry data) as well as high-frequency non-wind-driven motions such as inertial and tidal currents. Therefore, to allow identification of remaining non-wind-driven ageostrophic contributions, the energy levels contained in the drifting buoy total velocities and in the isolated ageostrophic currents are investigated by applying rotary spectral analysis on the different velocity data sets. Then the coherence to the wind stress is investigated using a vector cross-spectral analysis (VCSA) technique to study its frequency dependence [*Mooers*, 1970, 1973]. This method has been applied by *Davis et al.* [1981], *Daniault et al.* [1985], *McNally et al.* [1989], *Niiler and Paduan* [1995] and *Lee* [1996] to study wind-driven near-surface currents using the total current contained in drifting buoy data. Rotary analysis and VCSA allow evaluation of how well the wind-driven contribution can be isolated from the total observed current.

[6] The second step of the study is to use these high-frequency wind-driven currents together with the ECMWF (European Centre for Medium-Range Weather Forecasts) wind stress data to fit a wind-driven current model based on Ekman theory [*Ekman*, 1905]. According to Ekman's assumptions (steady, linear, vertically homogeneous ocean), the wind-driven surface velocity is found to be a solution of the so-called Ekman balance whose resolution depends on the parameterization of the turbulent stress. When the turbulent stress is chosen to be a function of the vertical velocity shear, assuming a constant eddy viscosity, the vertical structure of the Ekman currents is found to be a spiral. On the other hand, if the turbulent stress is written as a linear function of depth, the resulting wind-driven current is directed at 90° to the right (left) of the wind vector in the Northern Hemisphere (Southern Hemisphere) and its amplitude is constant through the Ekman depth. This is the so-called slab model. An instantaneous slab-like response of the mixed layer was found in many studies: In the MILE experiment, *Davis et al.* [1981] found the wind-driven currents to be consistent with a slab model of the mixed layer at inertial and daily periods. In the Atlantic, *Chereskin and Roemmich* [1991] found no slab-like behavior in the mixed layer but in a similar study in the Pacific *Wijffels et al.* [1994] used a more restrictive definition of the mixed layer depth and observed a 30- to 40-m slab layer above a high-shear transition layer. However, when averaging the velocity over longer periods, the vertical structure of the current appears to be very similar to the Ekman spiral [*Davis et al.*, 1981; *Weller*, 1981; *Price and Weller*, 1986; *Weller et al.*, 1991; *Rudnick and Weller*, 1993; *Wijffels et al.*, 1994; *Chereskin*, 1995; *Lee*, 1996; *Weller and Plueddemann*, 1996; *Schudlich and Price*, 1998]. *Davis et al.* [1981] explained this observed shear in the mean vertical profile by temporal variations in the mixed layer depth. In practice, the observed spirals are often flatter than in Ekman theory and appear to be more consistent with a diurnal cycle spiral [*Price and Weller*, 1986] whose amplitude decays faster than the vector rotates. This observed spiral results from modeling the upper ocean as an uniformly accelerated slab layer whose depth varies throughout the day. It is thus observed when averaging data over several days. *Niiler and Paduan* [1995] and *Ralph and Niiler* [1999] showed that a slab model underestimates the mixed layer depth. They deduced that the turbulent stress gradient could not be constant through the mixed layer as assumed by the slab model hypothesis, but rather had to decrease significantly with depth. *Ralph and Niiler* [1999] tested various models expressing the wind-driven velocity as a function of three parameters: the friction velocity due to surface stress, the Coriolis parameter, and the mean depth of the thermocline.

[7] For the present study we choose to model the wind-driven currents as a function of only wind stress and the Coriolis parameter, as in Ekman theory. The results obtained from this simple two-parameter model are then used to characterize and better understand the high-frequency response of near-surface currents to wind forcing.

[8] The outline of our paper is as follows: Drifter, altimetry and wind data are described in section 2, and their frequency content is analyzed in section 3. Section 4 presents the results of the vectorial correlation method. In section 5, the chosen model is presented. In section 6, results are analyzed in terms of phase, eddy viscosity, and Ekman layer depth. Furthermore, the spatial and seasonal variability of the model parameters is studied. Section 7 describes the map of Ekman currents applying the model to the wind stress data. Finally, a summary of the results and main conclusions are presented in section 8.

2. Data

2.1. Drifting Buoys

[9] We use data from satellite-tracked drifting buoys released from 1993 to 1999 as part of the WOCE (World Ocean Circulation Experiment) and TOGA (Tropical Ocean and Global Atmosphere) Surface Velocity Program (SVP). SVP buoys are surface floats tethered to a holey sock drogue centered at a depth of 15 m. These buoys were designed to reduce wind slippage and Stoke's drift [*Niiler et al.*, 1995] so that they closely follow the currents at their drogue's depth, above the seasonal thermocline. *Niiler et al.* [1987, 1995] estimated a downwind slip less than 1 cm/s in 10 m/s wind (wind climatological global mean). This accuracy is important for studying wind-driven currents mainly confined within the surface mixed layer. All raw data are quality controlled and processed at AOML (Atlantic Oceanographic and Meteorologic Laboratory). Position and velocity data are interpolated at AOML every 6 hours using a kriging method [*Hansen and Poulain*, 1996].

Table 1. Number of Drifting Buoys Released by Ocean and Hemisphere

Ocean	Hemisphere	Number of Buoys
Atlantic	North	974
Atlantic	South	305
Pacific	North	1207
Pacific	South	635
Indian	North	105
Indian	South	332

[10] Errors on velocities (ε_{buoy}) are less than 2–3 cm/s, taking into account both interpolation errors and residual signals due to the direct effect of wind-forcing on the surface float and nonlinear wave phenomena. All buoys carried a sensor for detecting the drogue loss. Only the trajectories of drogued buoys are selected in this study. This corresponds to more than 3500 buoys over the world ocean, distributed as shown in Table 1.

2.2. Altimetric Data

[11] We use Sea Surface Heights (SSH) from ERS-1 and ERS-2 and TOPEX/POSEIDON for the period 1993–1999. Usual altimetric corrections are applied [*Le Traon et al.*, 1998] so that altimetric heights are obtained with a precision of 3–4 cm. Because of the lack of an accurate geoid at small spatial scales, absolute dynamic topography values cannot be directly inferred from the SSH data. Instead, along-track sea level anomalies (SLA) relative to a 7-year (1993–1999) mean profile are computed.

[12] We use a multivariate objective analysis to merge ERS-1 and ERS-2 and T/P SLAs and compute geostrophic velocity anomalies and associated errors (ε_{alti}) along the drifters' trajectories [*Hernandez et al.*, 1995]. This method, based on geostrophic assumptions, fails close to the equator. Velocities are computed at each drifter's position with an absolute latitude higher than 3°, and we leave out the equatorial band from our investigations. Absolute geostrophic surface velocities are then computed adding a mean dynamic velocity field to the velocity anomalies. The mean dynamic velocity field used was computed using a synthetic method described for the North and tropical Atlantic Ocean by *Rio and Hernandez* [2002] and extended to the world ocean. This method was adapted from the so-called "synthetic geoid" method [*Mitchell et al.*, 1990; *Glenn et al.*, 1991]. It consists in subtracting synoptically the altimetric anomaly field (deduced from TOPEX and ERS-1 and ERS-2 satellites for the 1993–1999 period) to in situ measurements of the full dynamical signal (buoy's velocities from the international WOCE-TOGA program and XBT, CTD cast over the same period). These differences provide local estimates of the mean field in term of currents or dynamic topography and the mean dynamic topography over the entire North Atlantic is then obtained using an inverse technique. Compared to classical climatological fields, this field contains smaller scales of the mesoscale range and reproduces the strong current areas better.

2.3. Wind Data

[13] The wind data used for this study are 6-hourly analyzed wind surface stresses from the European Centre for Medium-Range Weather Forecasts (ECMWF). As for drifters and altimetry SSH, the data span the period 1993–1999. They are provided on a 1° grid until February 1998 and on a 0.5° grid afterward. Stress values were bilinearly interpolated to the drifters' positions in order to provide high-frequency wind stress time series along the buoys' trajectories.

2.4. Data Quality

[14] To check the quality of the data, we looked at the wind stress data and the drifting buoy data available from July to November 1993 in the Azores area as part of the SEMAPHORE-93 experiment [*Hernandez*, 1995]. SEMAPHORE wind stress data consist of buoy and ship observations combined with data from the ERS-1 scatterometer. SEMAPHORE drifting buoy data consist of 24 BODEGA (SVP-like) buoys (to which no kriging has been applied), also present in the WOCE data set.

[15] It results from this study that correlation between drifting velocities and wind stress is enhanced when using higher-quality wind stress data (such as SEMAPHORE wind stress fields). Moreover, the smoothing applied on our data set by kriging deteriorates the correlation to the wind stress. These results will have to be considered for the forthcoming analysis.

3. Spectral Analysis

[16] The goal is to quantify the distribution of energy in the data and to assess its origin to extract properly the wind-driven current using both the drifting buoy and altimetry information.

3.1. Rotary Spectra

[17] The rotary spectral energy density components of the data are analyzed in this section. Time series of velocity and wind for each individual drifter are cut into 4-month pieces. Then they are gathered into three latitudinal bands (in terms of absolute latitude) in order to separate the latitude-dependent inertial oscillations. The number of 4-month-long series obtained for each latitudinal band over the globe is summarized in Table 2.

[18] We display in Figure 1 the cyclonic and anticyclonic spectra of the near-surface total velocity vector measured by drifting buoys and those of the ageostrophic velocity obtained by subtracting the altimetric velocities as computed in section 2.2 from the drifting buoy velocities. The wind stress spectrum is displayed for the anticyclonic component and the cyclonic component. Cyclonic frequencies corre-

Table 2. Number of 4-Month-Long Series by Latitude Bands[a]

	$3° < \|\text{Latitude}\| < 15°$	$15° < \|\text{Latitude}\| < 30°$	$30° < \|\text{Latitude}\| < 90°$
Corresponding inertial period	2–10 days	1–2 days	12 hours to 1 day
Number of series	526	847	1334

[a]Southern and Northern latitude bands were combined.

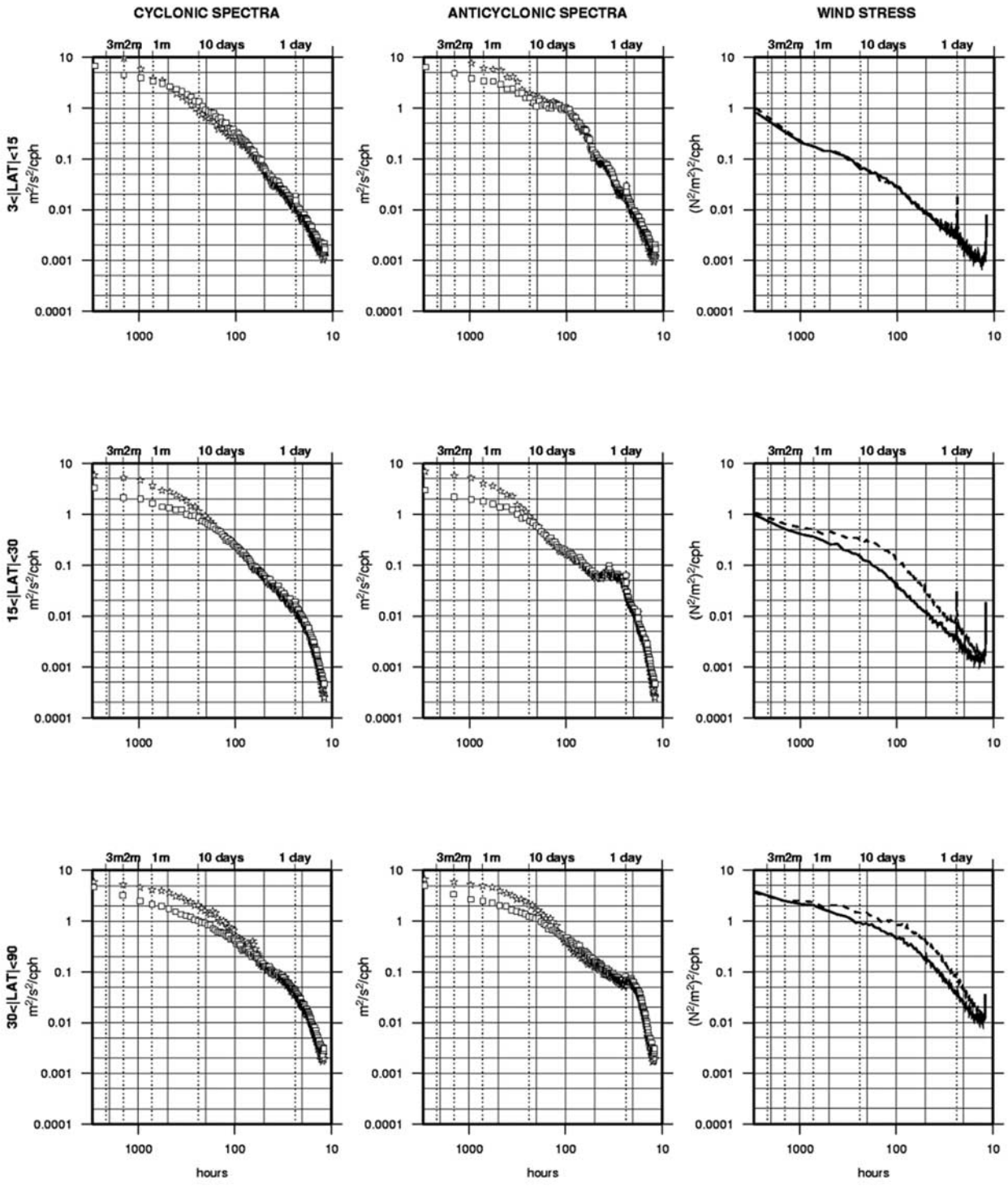

Figure 1. Rotary spectra of the drifter velocities (stars), its ageostrophic component (squares) and the wind stress (anticyclonic (dashed line) and cyclonic motion).

spond to counterclockwise (clockwise) movements in the Northern (Southern) Hemisphere, while anticyclonic frequencies correspond to counterclockwise (clockwise) movements in the Southern (Northern) Hemisphere.

3.1.1. Rotary Spectra of the Wind Stress

[19] The wind stress rotary spectra show a quite similar pattern at middle and high latitudes with spectral levels significantly higher at anticyclonic frequencies than at cyclonic frequencies for periods smaller than 1 month. At low latitudes (between 3° and 15° north and south), anticyclonic and cyclonic spectra exhibit the same energy level.

3.1.2. Rotary Spectra of the Near-Surface Currents

[20] The spectra of the total velocity were obtained by averaging individual buoy spectra over the specified latitude

range (star dotted line in Figure 1). For the anticyclonic spectra, the energy levels corresponding to diurnal tidal currents and inertial oscillations are clearly separated from the energy contained at other frequencies. Indeed, for each latitudinal band, a spectral hole (i.e., a spectral band with less energy) is observed, separating the mesoscale structure low-frequency domain from the internal wave high-frequency domain. At low latitudes ([3°–15°]), it occurs at a period of around 10 days since inertial oscillations are widespread all over the 2 days (at ±15° latitude) to 229 hours (at ±3° latitude) period range of the anticyclonic spectra. The spectral hole is visible at a 40-hour period for the [15°–30°] latitude range, and at a 1-day period for the [30°–90°] latitude range.

[21] On the cyclonic spectra, the intensity of the peak associated to the diurnal tidal period may be smoothed by the fact we consider data over a long period and a large area. We want to separate the wind-driven current from the buoy drift signal using the altimetric information on the geostrophic current. To estimate the contribution to the spectra of the geostrophic velocities deduced from altimetry, we first compute the spectra of the ageostrophic circulation (square dotted line) estimated by removing the geostrophic velocities from the drifter velocity time series. The geostrophic energy contribution is the difference between the star dotted line (geostrophic + ageostrophic velocities) and the square dotted line (ageostrophic velocities).

[22] Because neither the tidal nor the inertial energies are contained in the geostrophic altimetric velocities, the rotary spectra associated with the ageostrophic velocities still contain the high energy levels of tidal and inertial oscillations. At middle and high latitudes [15°–90°], tidal and inertial oscillations are confined to high frequencies (periods smaller than 2 days) so that they can be clearly separated from the lower-frequency, geostrophic motions depicted by altimetry. In the [30°–90°] latitude range, important differences between the total spectra and the ageostrophic spectra are observed for anticyclonic and cyclonic periods longer than 100 hours (~4 days). Up to half of the total energy is contained in the geostrophic signal. In the [15°–30°] latitude range, a clear difference between the energy associated to the total signal and the ageostrophic signal occurs for cyclonic and anticyclonic periods longer than 10 days. In that case, more than half the total energy is found to be contained in the geostrophic signal.

[23] For the lowest latitude band [3°–15°], an important part of the total energy is found to be contained in the geostrophic signal for anticyclonic periods longer than 10 days. However, for cyclonic periods, subtracting the altimetric signal from the total drift rather adds noise into the velocity time series, as the resulting ageostrophic energy is found to be larger than the total energy for periods smaller than a month. The interpolation of altimetric heights into altimetric velocities is based on geostrophic assumptions, which have to be carefully handled when getting closer to the equator (the Coriolis parameter F tends toward 0). Thus, at low latitudes, the interpolation error can get larger than the physical signal it is mapping, with a resultantly poor signal-to-noise ratio.

[24] To conclude, the spectral study highlights the high energy level contained in the geostrophic part of the drift time series at middle and high latitudes. An important contribution is obtained for periods greater than 10 days in the [15°–30°] latitude range and greater than 4 days in the [30°–90°] latitude range. For those latitudes, the geostrophic information contained in the altimetric signal needs to be removed to extract the wind-driven currents from the total drifter velocities.

[25] However, at subinertial periods, most of the total energy level is contained in ageostrophic phenomena like tides and inertial oscillations. We will see in the next section that these ageostrophic phenomena, which are not wind-driven, contaminate the high-frequency wind coherent signals so that they have to be removed from the drifter velocities as well.

3.2. Cross-Spectral Analysis

3.2.1. Wind and Total Current Cross Spectra

[26] Figure 2 shows the results of the cross-spectral analysis between the wind stress and the total current as given by drifter velocities. Negative (positive) frequencies describe anticyclonic (cyclonic) movements. Negative phases between the two vectors indicate than the current is directed to the right (left) of the wind stress direction in the Northern (Southern) Hemisphere.

[27] All latitudes display higher coherences in the anticyclonic domain than in the cyclonic domain. This was observed in previous studies [*Poulain*, 1990; *Hernandez*, 1995]. At frequencies lower than the inertial frequency, anticyclonic waves are trapped by planetary vorticity and cannot dissipate by wave propagation as cyclonic structures do [*Gonella*, 1972]. At higher frequencies, where there is no trapping, the higher anticyclonic wind coherence observed might be rather related to the higher energy density levels in the anticyclonic part of the wind stress rotary spectra (Figure 1). Coherences remain low, below 0.5 at all latitudes. However, the Southern Hemisphere seems to exhibit larger coherences than the Northern Hemisphere (not shown) and better coherences are obtained when focusing on particular regions (up to 0.7 in the Southern Atlantic, for instance). The spatial variability of the relationship between currents and wind stress will be analyzed later in section 4.

[28] At periods greater than both the tidal and inertial periods, the phase relationship is consistent with the theory described by *Gonella* [1972]. In the Northern (Southern) Hemisphere, near-surface currents are directed to the right (left) of the wind stress at frequencies higher than the inertial frequency $-f$. At frequencies lower than $-f$, the phase becomes positive. On Figure 2, a theoretical phase relationship is superimposed on the observations. This was computed taking the mean inertial frequency of the latitude range. This corresponds to $f = -0.01$ in the [3–15] range, $f = -0.03$ for the [15–30] range and $f = -0.06$ for the [30–90] range. However, in each case, data are spanned all over the latitude range so that we observe a smooth change in phase direction around the anticyclonic mean inertial frequency. In the frequency range where coherence is highest, the phase relationship is quite stable, in the $-30°$ to $-60°$ range. This corresponds to periods longer than 10 days at low latitudes and to anticyclonic periods longer than 1 day and cyclonic periods greater than 10 days in the [15–30] latitude range. Poleward of 30°N or 30°S,

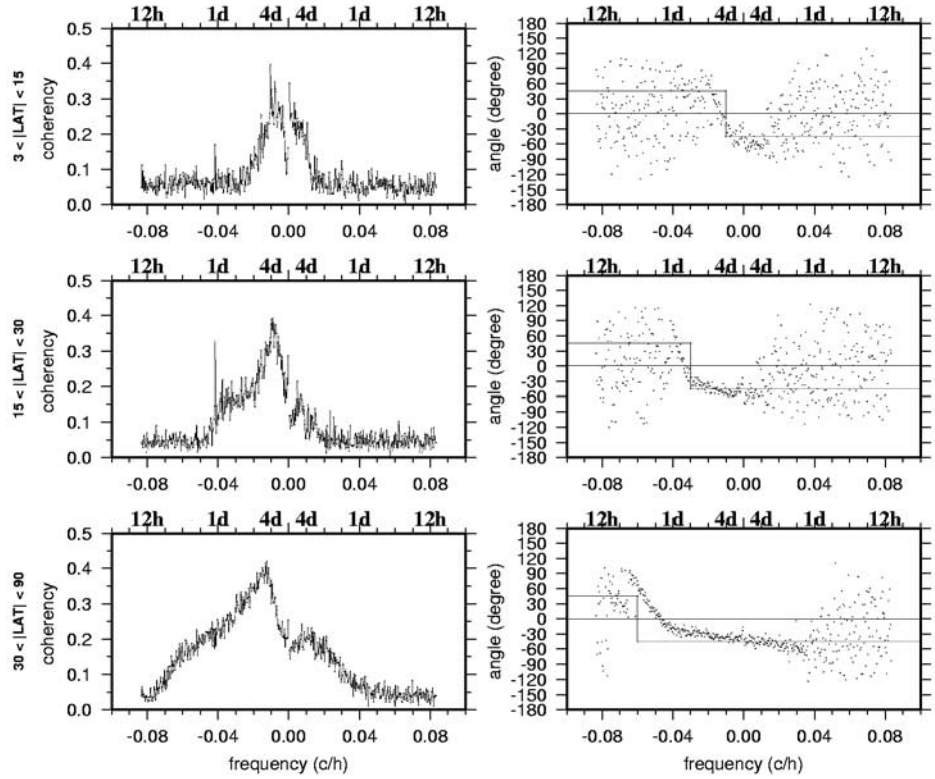

Figure 2. Cross-spectral analysis between the total drifter velocity and wind stress. Solid line in the right panels figures the theoretical phase relationship [*Gonella*, 1972].

the phase relationship is in quite good agreement with the theory, except for cyclonic periods shorter than 1 day and anticyclonic periods close to 12 hours. Outside of these period ranges, the phase distribution scatters and coherences are low. This is due to the high energy level contained in the inertial oscillations that overwhelms the wind coherent signal, but also to the temporal resolution (limited to 6 hours for both drifting buoy and wind stress data) and the poor quality of the data used at those frequencies.

3.2.2. Wind and Ageostrophic Current Cross Spectra

[29] The results of the cross-spectral analysis between the drifter velocities (star dotted line for the total velocity field) and the wind stress data are now displayed in Figure 3 for the anticyclonic (negative frequencies) and cyclonic (positive frequencies) relationship on a logarithmic scale to consider periods longer than 2 days. The spectral analysis computed between the ageostrophic velocity field and the wind stress is superimposed on the first results (square dotted line) to investigate the contribution of the altimetry-deduced geostrophic field in enhancing the wind coherence.

[30] As expected, removing the geostrophic velocities from the total current field improves the wind coherence at all frequencies where the geostrophic signal was shown to contain a major part of the total energy (see section 3.1.2). On the other hand, no improvement is observed for cyclonic movements at low latitudes. At middle and high latitudes, significant improvements are observed for both cyclonic and anticyclonic movements. At these latitudes, the ageostrophic signal obtained better describes the near-surface current response to wind stress.

[31] However, the maximum coherences obtained remain rather weak (best values are obtained in the Southern Hemisphere (not shown) but are below 0.5). This may be due to errors in the wind stress field used for the study (section 2.4), to the ageostrophic acceleration term not related to the wind and finally to the cumulative error associated with the estimation of the buoys geostrophic velocity (including errors associated with the mean dynamic velocity field used to compute absolute altimetric velocities, errors due to the difficulty of reproducing the entire geostrophic signal from altimetry in areas where gradients are strong and/or scales are small and errors due to the estimation of velocity anomalies from the altimetric signal [*Le Traon and Dibarboure*, 2002]). This can result in a residual geostrophic signal in the estimated wind-driven current. Besides, no clear improvement is obtained for periods shorter than tidal and inertial periods.

3.3. Conclusion: Extracting the High-Frequency Wind-Driven Current From Drifting Buoy Velocities

[32] As expected, removing an estimate of the geostrophic current from drifter velocities enhances the wind-coherent signal. Overall, the best improvements are obtained for periods longer than 10 days. On the other hand, the coherence between the ageostrophic velocities and wind stress data is found to be highest for periods shorter than 20 days and to drop at near- and sub-inertial periods where the wind-driven current is overwhelmed by inertial and tidal

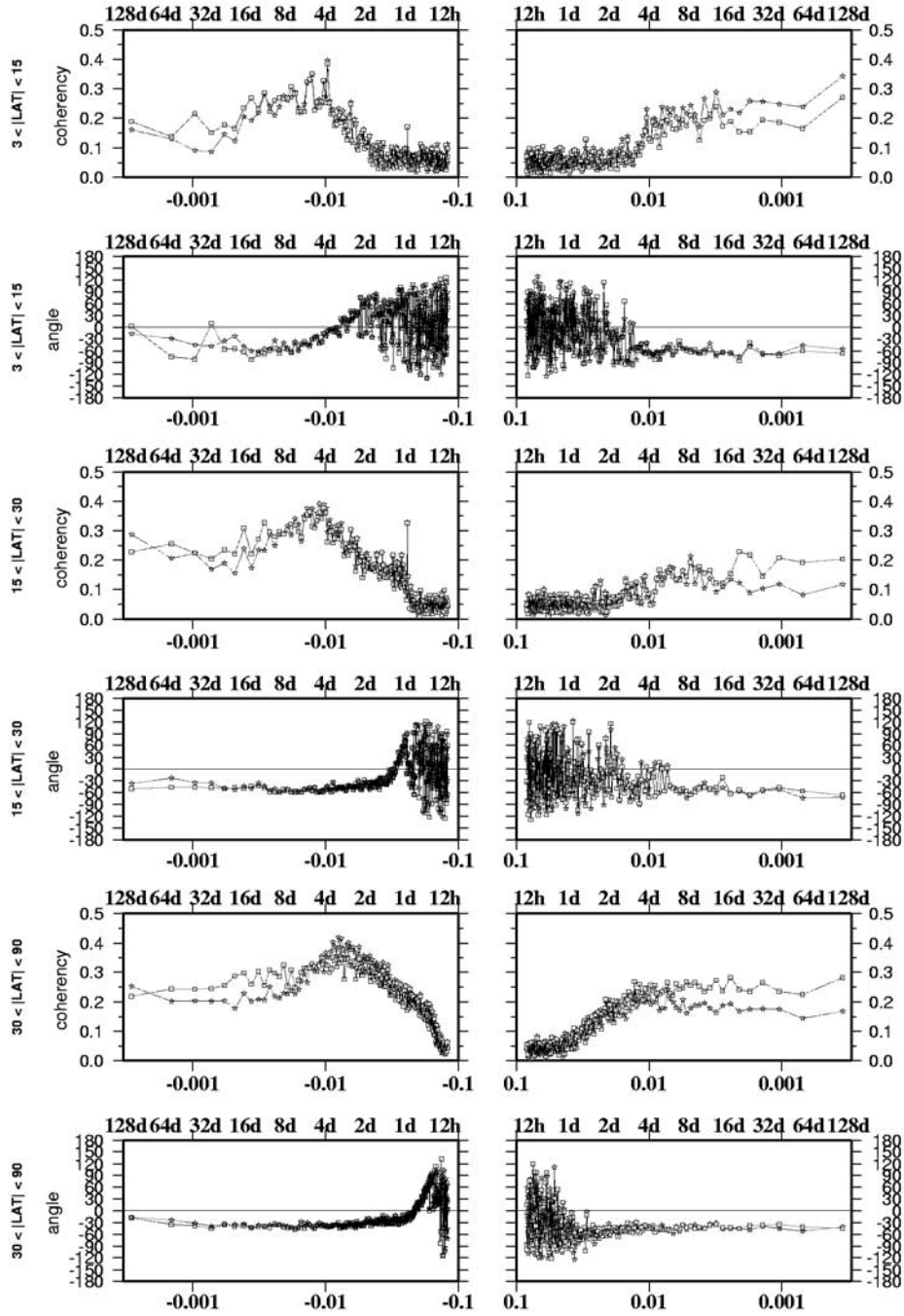

Figure 3. Cross-spectral analysis between the total drifter velocity and the wind stress (stars) and between the ageostrophic part of the drifter velocity and the wind stress (squares) for the cyclonic (right) and anticyclonic (left) relations.

signals and where uncertainties on the wind stress and drifting buoy data quality increase. Maximum coherence is observed at about 4 days for the anticyclonic part.

[33] Thus, according to the spectral analysis described in the previous two paragraphs, to estimate the wind-driven part of the currents from the drifting buoy data, we first subtract the geostrophic velocities deduced from altimetry. Then, to remove the tidal and inertial components of the ageostrophic velocities, a low-pass filter is applied along the buoy trajectories. For each trajectory, the maximal inertial period is computed. Then the cut-off period (P_{low}) is chosen as the highest value between this inertial period and the diurnal tidal period (24 hours). Finally, to analyze the high-frequency part of the wind-driven current, we filter data for periods longer than 20 days and thus focus on the [P_{low}, 20 days] period range, where the coherence to the wind was found to be maximal. This band-filtered ageostrophic current will be referred to as the high-frequency wind-driven current, and will be used in the next three sections, together with similarly filtered

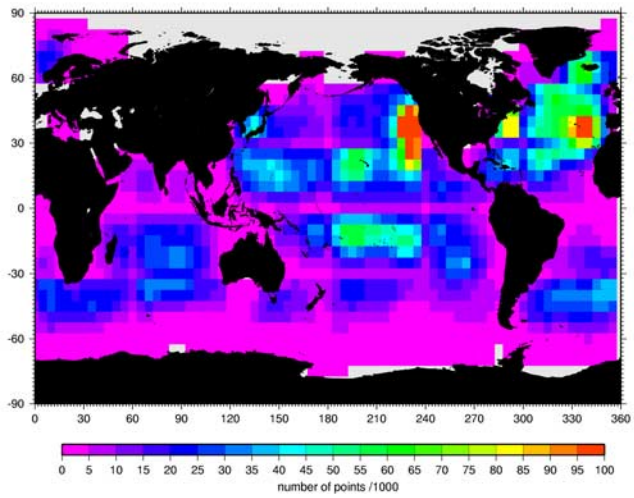

Figure 4. Number of data used at each 5° × 5° grid point.

ECMWF wind stress fields, to model the high-frequency Ekman currents of the upper surface layer.

4. Vectorial Correlations

[34] A first way to analyze the relationship between the high-frequency wind-driven current computed in section III and the wind stress is to use two dimensional correlation approach developed by *Vialar* [1978]. In this approach, the correlation coefficient and angle between two vector series are estimated through a least squares method. This is done for all data contained within a 7° radius domain around each point of a 5° latitude × longitude grid. This 5°- resolution grid is used to obtain for each domain a representative number of data (see Figure 4). The data are not quite evenly distributed over the different basins and this will have a direct impact on the accuracy of our results. In fact, the spatial coverage obtained is weaker at high latitudes where results should be carefully interpreted. On the other hand, the results will be statistically meaningful for the northern Atlantic, the tropical Pacific, the northeastern Pacific and at midlatitudes in the South Atlantic and the south Indian Ocean, where the data coverage is good. Results obtained are displayed in Figure 7.

[35] Correlation values are consistent with the spectral coherences obtained in the previous cross-spectral analysis. However, results show significant spatial variability. In each basin, correlations are lower in the tropical band than at higher latitudes. Good correlations (0.4–0.7) are obtained in the Northern Pacific and south of −30° latitude for all oceans. Weaker correlations (<0.2) are obtained in regions where the mesoscale variability is known to be high (Gulf Stream, Kuroshio, Agulhas current). The altimetric signal does not reproduce entirely the high gradients associated with these regions, so a residual geostrophic signal might be contained in the high-frequency velocity computed in section 3.

[36] In agreement with the Ekman theory, angle correlation values are negative in the Northern Hemisphere (which corresponds to a near-surface current to the right of the wind stress direction) and positive in the Southern Hemisphere (near-surface current to the left of the wind stress direction). In both hemispheres the angle clearly decreases with latitude, from 70°–90° near the equator to 20°–40° in subpolar regions. This result can be explained by the position of the 15-m-level drifter measurements inside an Ekman spiral; the ocean stratification (as computed for instance from *Levitus* [1982] climatology) is stronger at low latitudes than at high latitudes. Therefore the Ekman layer is deeper at high latitudes so that the 15-m drifter velocity will sample a shallower level of the presumable Ekman spiral than at low latitudes, resulting in a smaller angle.

5. Modeling Ekman Currents

5.1. Ekman Balance

[37] Ekman theory of wind-driven currents is based on the momentum equation for a steady, linear and vertically homogeneous ocean, away from horizontal boundaries under steady wind stress conditions,

$$-fu + \frac{1}{\rho}\frac{\partial \tau_y}{\partial z} = \frac{1}{\rho}\frac{\partial p}{\partial y} \qquad f\nu + \frac{1}{\rho}\frac{\partial \tau_x}{\partial z} = \frac{1}{\rho}\frac{\partial p}{\partial x},$$

where ρ is the density, p is pressure, f is the Coriolis parameter, τ is the turbulent wind stress, and u and v are, respectively, the zonal and meridional current velocities. Near-surface current velocity (u, v) can be written as the sum of the geostrophic pressure-driven flow (u_g, v_g) and the wind-driven (Ekman) flow (u_e, v_e).

$$-fu_g = \frac{1}{\rho}\frac{\partial p}{\partial y} \qquad f\nu_g = \frac{1}{\rho}\frac{\partial p}{\partial x}$$

$$-fu_e = \frac{1}{\rho}\frac{\partial \tau_y}{\partial z} \qquad f\nu_e = -\frac{1}{\rho}\frac{\partial \tau_x}{\partial z}.$$

To solve the last equations, the so-called Ekman balance, a parameterization of the turbulent stress is necessary.

5.2. Parameterization of the Turbulent Stress

5.2.1. Ekman Solution

[38] *Ekman* [1905] chose to write the wind stress as a function of the vertical shear of horizontal velocity using a constant eddy viscosity ν,

$$\vec{\tau} = \rho\nu\frac{\partial \vec{U}_e}{\partial z}$$

where $\vec{U}_e = (u_e, v_e)$.

[39] He deduced the classical Ekman solution for wind-driven currents,

$$u_e = Ue^{\frac{z}{D_e}}\cos\left(\frac{z}{4} + \frac{z}{D_e}\right) \qquad \nu_e = Ue^{\frac{z}{D_e}}\sin\left(\frac{\pi}{4} + \frac{z}{D_e}\right) \quad (1)$$

$$U = \frac{\tau_0}{\rho\sqrt{(\nu f)}} \qquad D_e = \sqrt{\frac{2\nu}{f}}, \quad (2)$$

so that the vertical structure of the Ekman currents is a spiral rotating clockwise (anticlockwise) with depth in the North-

ern (Southern) Hemisphere, with a surface current directed at 45° to the right (left) of the wind in the Northern (Southern) Hemisphere and a current in the opposite direction at the depth D_e. At that depth, the amplitude of the Ekman current is 4% of the amplitude of the surface current.

5.2.2. Slab Model

[40] Observational confirmation of this theoretical spiral has always been very hard to obtain. Observations tend to feature a mixed layer in which nearly homogeneous momentum is maintained by turbulent overturning driven by wind, surface waves and Langmuir circulation. In that context, *Pollard and Millard* [1970] suggested writing the turbulent stress as a linear function of depth,

$$\tau(z) = \frac{\tau_0}{H} z + \tau_0,$$

where τ_0 is the surface stress and H is the depth at which the turbulent stress vanishes.

[41] The resulting wind-driven current is directed at 90° to the right (left) of the wind vector in the Northern Hemisphere (Southern Hemisphere) and its amplitude U is constant through the Ekman depth H,

$$U = \frac{\tau_0}{\rho f H}.$$

This is the so-called slab model, the mixed layer acting as a slab, i.e., as a strong turbulence layer where density and velocity are homogeneous and where consequently no Ekman spiral can be observed.

5.3. Model Used

[42] We consider the three-parameter (a, b, c) models proposed by *Ralph and Niiler* [1999],

$$U = \frac{\tau}{\rho f H_*} = \beta \tau^a f^b D_T^c,$$

where H_* is the depth scale for the turbulent stress and D_T is the depth of the top of the thermocline. Their study indicates that it is not clear whether D_T is a relevant scale. So in our study, we choose $c = 0$ and test the two following models: The first one (M1),

$$\vec{u}_a = \frac{b\,\vec{\tau}}{\sqrt{f}} e^{i\theta},$$

is consistent with Ekman scaling (equations (1) and (2)). This model explained 37% of the variance in *Ralph and Niiler* [1999] data. The second one (M2),

$$\vec{u}_a = \frac{b'\,\vec{\tau}}{\sqrt{f|\tau|}} e^{i\theta'},$$

results from the consideration that the eddy viscosity ν is no longer constant but is a function of the turbulent stress [*Santiago-Mandujano and Firing*, 1990]. This model explained 49% of the variance in *Ralph and Niiler* [1999] data.

[43] The goal of the next section is to determine the parameters b and θ (b' and θ') for model M1 (M2) using estimates of the high-frequency wind-driven current computed in section 3 for $\vec{u}_e$ and the high-frequency ECMWF wind stress data for $\vec{\tau}$. Then, through equation (2), values of the Ekman depth D_e (m) and eddy viscosity ν (m^2/s) can be directly deduced from the b or b' parameter.

6. Results

[44] We applied the two previous models to the high-frequency wind-driven currents derived as explained in section 3. Here b, the amplitude factor, and θ, the phase difference between the wind-driven currents and the wind stress, are determined through a least squares minimization applied to the data contained within a 7° radius domain around each point of a 5° latitude × longitude grid, like for the computation of vectorial correlations (section 4).

6.1. Model 1

[45] The model parameters b and θ were determined by a least squares fit to the data. Estimation errors were computed using a Monte-Carlo method [*Kalos and Whitlock*, 1986]. The standard deviation (std) of the input noise in the drifter velocities is taken as 30% of the mean velocity value. For the phase, a 10° std noise is chosen. Parameter values and estimation errors are displayed on Figure 8.

6.1.1. Phase Parameter θ

[46] The θ values are very similar to the correlation angle values described in section 4 (Figure 7). Errors on estimations of θ are very small, less than 1° in most areas. Comparing our results to other studies is not an easy task, since few are based on data sets longer than 1 year, so most of them are biased toward a season or a particular event. Using a slab model and data from 1987 to 1994, *Ralph and Niiler* [1999] found $\theta = 55° \pm 5°$ for the Pacific tropical band [−30°; 30°]. In the same region, *Lagerloef et al.* [1999] found a 60°−70° angle using data from October 1992 to December 1994. In that region we find angles ranging from 40° to 60° in the Northern Hemisphere and −50° to −70° in the Southern Hemisphere. More comparisons will be done in section 6.3, where we will study the seasonal variability of the current response.

6.1.2. Amplitude Parameter *b*

[47] Error estimates are always less than 10% of the parameter value, which is small given the chosen standard deviation of the input noise (30% of the mean velocity value).

[48] Like θ, the b parameter exhibits significant spatial variability. Its value ranges from 10^{-3} m^2 kg^{-1} $s^{1/2}$ in the northern Atlantic and Pacific to $2-3\ 10^{-3}$ m^2 kg^{-1} $s^{1/2}$ in the southern subpolar latitudes and to $4-5\ 10^{-3}$ m^2 kg^{-1} $s^{1/2}$ in the tropical band. Comparatively, *Ralph and Niiler* [1999] found $b = 9\ 10^{-3}$ m^2 kg^{-1} $s^{1/2}$ for the entire tropical Pacific (latitudes between −30° and 30°). The data and method used in their study differ from ours on many points, which can explain part of the large difference observed: First, they used data spanning the years 1987 to 1994, while we are considering data from 1993 to 1999. Then they filtered their data for periods shorter than 5 days (computing 5-day averaged velocities), while we focus on the high-frequency part of our data (periods shorter than 20 days and longer than both the tidal and inertial period). Also, they used both the ECMWF wind stress data and a

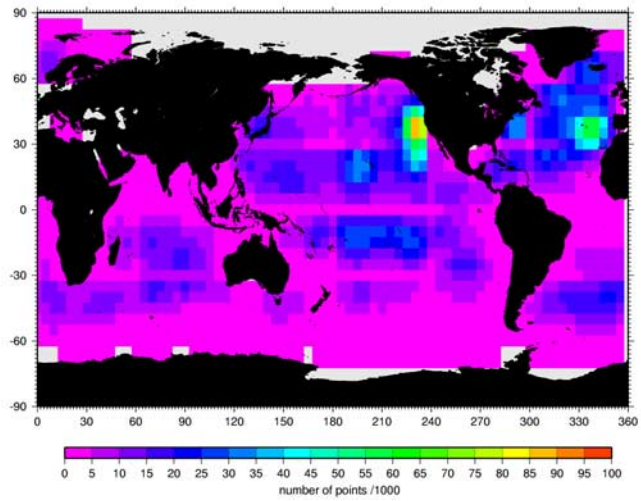

Figure 5. Number of data used at each 5° × 5° grid point (only winter data).

wind data set computed using SSM/I (Special Sensor Microwave Imager) wind observations and described by *Atlas et al.* [1996].

6.1.3. Percentage of Variance Explained by the Model

[49] Figure 9 gives the percentage of variance explained by the model for the zonal and meridional components of the velocity. Values are consistent with the vectorial correlations obtained in section 4. Indeed, less than 5% of the variance is explained in regions where the correlation between the wind stress and the ageostrophic velocity is weak (Kuroshio, Gulf Stream, Gulf of Mexico, the tropical central Pacific, and the east coast of South Africa and South America.)

[50] In the tropical band, values are small but higher values are obtained for the zonal velocity component (4 to 10% of the variance explained) than for the meridional component (variance explained lower than 6%).

[51] In the North Atlantic, 10–20% of variance is explained for the zonal velocity and 4–10% for the meridional component. The largest values are obtained in the North Central Pacific (20–25% for the zonal component, 20–30% for the meridional component), in the South Atlantic (20–40% for the zonal component, 10–30% for the meridional component) and south of −30° latitude in the Pacific and Indian Oceans (where the percentage of variance explained can reach 30–40%). These values may be highly dependent on the quality of the wind stress data and the estimation of the wind-driven currents, as for the correlation results (section 2.4).

6.2. Model 2

[52] Contrary to the *Ralph and Niiler* [1999] study, we found no significant differences between model 1 and model 2 in terms of percentage of variance explained. Model 2 assumes a dependence of eddy viscosity on turbulent stress, whereas model 1 considers eddy viscosity as a constant. The high temporal coverage of our data (the results obtained take into account processes present in a 7-year time series) and the relatively low spatial resolution of the chosen grid (we fit the models on 7° radius domains, whereas *Ralph and Niiler* [1999] considered the whole Pacific tropical band) may result in no significant differences for this data set when considering the eddy viscosity as a constant or dependent on the turbulent stress. We therefore choose to focus on the results obtained using the first model.

6.3. Seasonal Variability

[53] To study the seasonal variability of the wind-driven response, we now consider separately the winter data (from October to March) and the summer data (from April to September). These extended seasons were chosen considering the seasonal cycle of the sea surface temperature (showing a minimum in February and a maximum in September in the Northern Hemisphere). As shown in Figures 5 and 6, the number of data points for each grid point is comparable in both cases. Figure 10 and Figure 11 show the global distribution of the b and θ parameters, respectively, for the boreal winter (austral summer) and boreal summer (austral winter). To better analyze values of the b parameter and understand its variability, we also show the corresponding values of Ekman Depth and Eddy Viscosity computed using equation (2).

$$U = \frac{\tau}{\rho\sqrt{\nu f}} = \frac{b\,\tau}{\rho\sqrt{f}} \Leftrightarrow \nu = \frac{1}{\rho^2 b^2} \tag{3}$$

$$D_e = \sqrt{\frac{2\nu}{f}} \Leftrightarrow D_e = \frac{\sqrt{2}}{b\rho\sqrt{f}} = \sqrt{2} \times H_*. \tag{4}$$

As all values feature a fairly zonal distribution, we computed in Figure 12 for each ocean a longitudinal mean value as a function of latitude. A striking result is that both θ and b (and as a result, also D_e and A_z) exhibit a high seasonal variability.

6.3.1. Phase Parameter θ

[54] In the northern Indian Ocean, values are in the range −50 to −60° in winter (Figure 10) and −70 to −90° in summer (Figure 11). In the northern Pacific and Atlantic Oceans, the range is −15 to −50° in winter (Figure 10) and

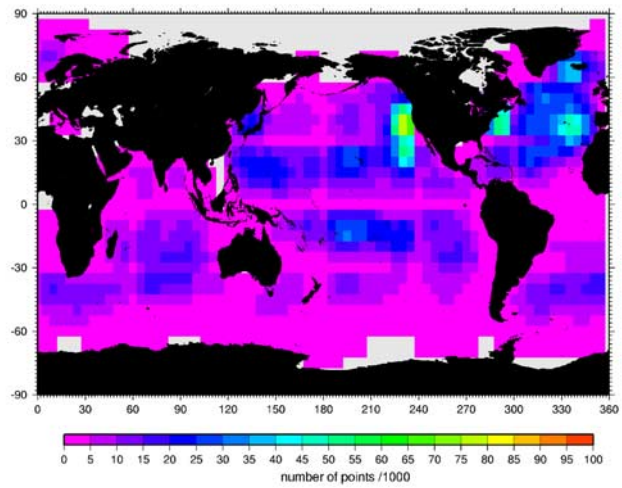

Figure 6. Number of data used at each 5° × 5° grid point (only summer data).

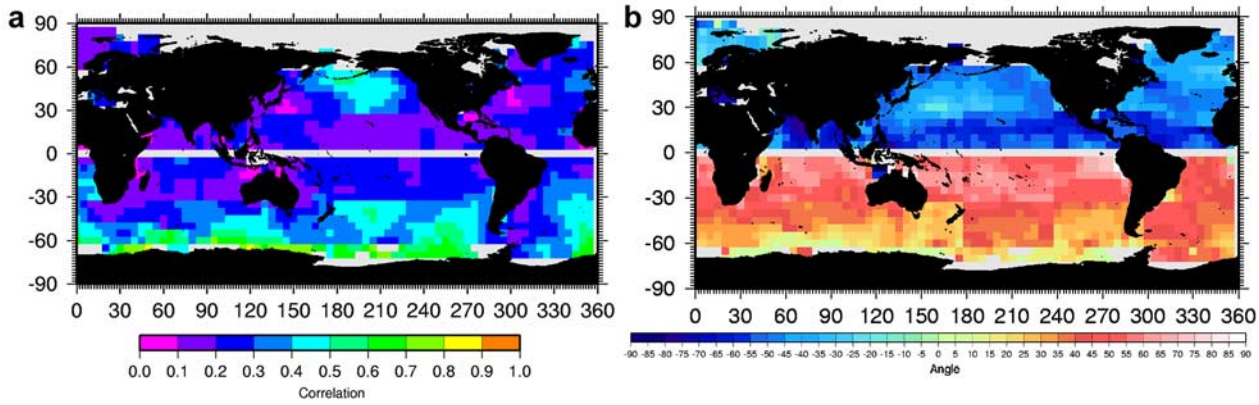

Figure 7. Vectorial correlation between drifter ageostrophic velocities and wind stress.

−50 to −80° in summer (Figure 11). In the Southern Hemisphere, values range from 10° to 50° in winter and from 50 to 90° in summer, with noticeable differences between the three oceans; θ is much lower in winter than in summer for all basins and latitudes. The reason might be the same as that given for the spatial variability of θ, i.e., the seasonal variations of the stratification, so that in winter the velocity sampled by the 15-m drifter corresponds to a higher level in the Ekman spiral. The angle between the velocity vector and the wind stress vector will be closer to the surface angle.

[55] *Schudlich and Price* [1998] used observations from the Long-Term Upper Ocean Study (LOTUS) in the western Sargasso Sea from May 1982 to February 1983. They found that the near-surface current was directed at 78° to the right of the wind in summer, 43° in winter. In that particular region we find similar angles (30°–40° in winter; 60°–70° in summer).

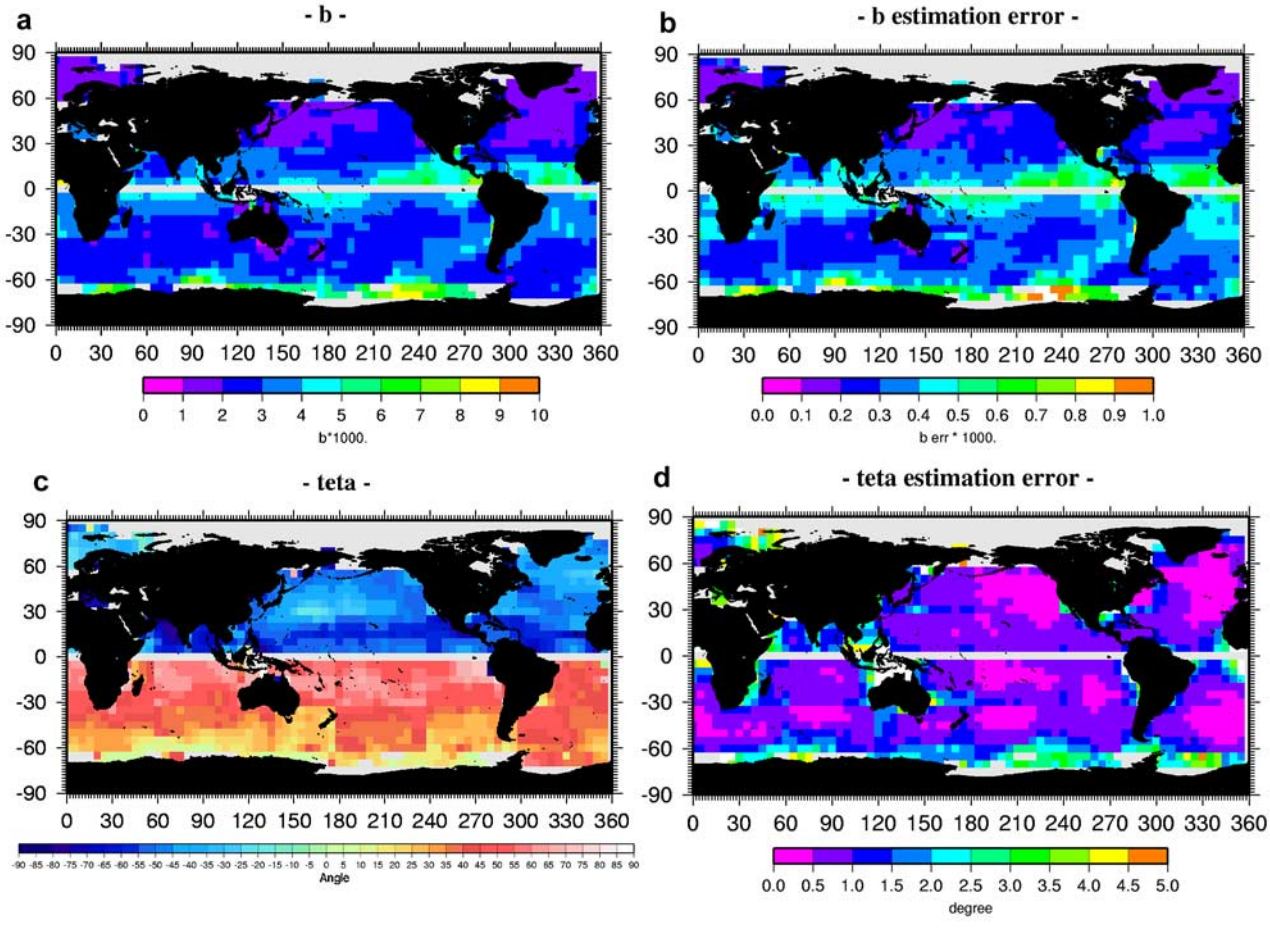

Figure 8. (a, b) Amplitude (*b*) and (c, d) phase (teta) parameters and estimation errors.

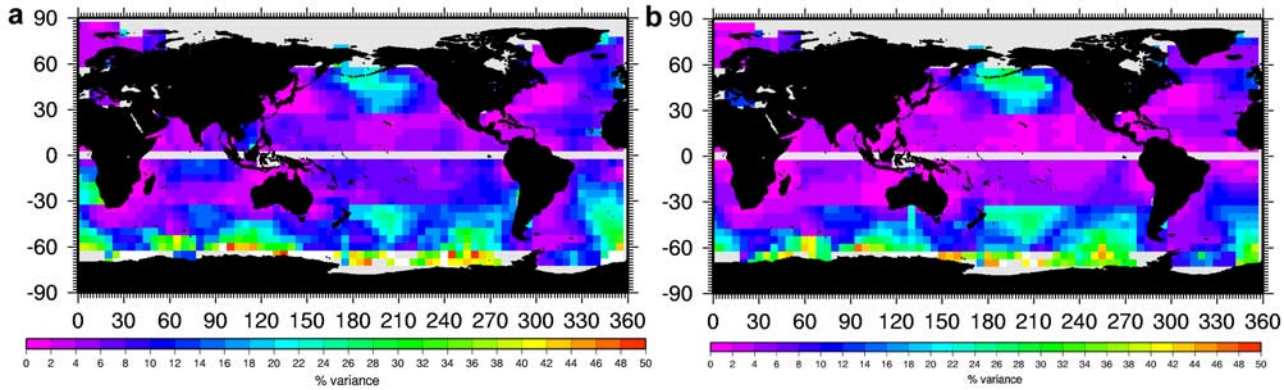

Figure 9. Percentage of variance explained by the model for (a) zonal and (b) meridional velocities.

[56] Near the coast of California, *Price and Weller* [1986] found an angle of 60° to the right of the wind during spring 1980 (April–May). In the same region, we find an angle of 57.6° to the right of the wind.

[57] In the northeast Pacific, *Niiler and Paduan* [1995] modeled the wind-driven current in fall 1987 and winter 1989–1990 as having an angle of 70° to the right of the wind. Using the same data set, *Meurs and Niiler* [1997] found an angle equal to 56.4° for the year 1987 and to 61.8° for the year 1989. For that region we find a smaller angle (48°).

[58] The discrepancies obtained between the various studies are quite expectable. They are related to the diversity of the data used (differences in quality and physical content), the various models chosen and the interannual variability of the wind forcing. Indeed, most studies focus on a short period; by considering the whole seven-year data range, we cancel out the special features of individual

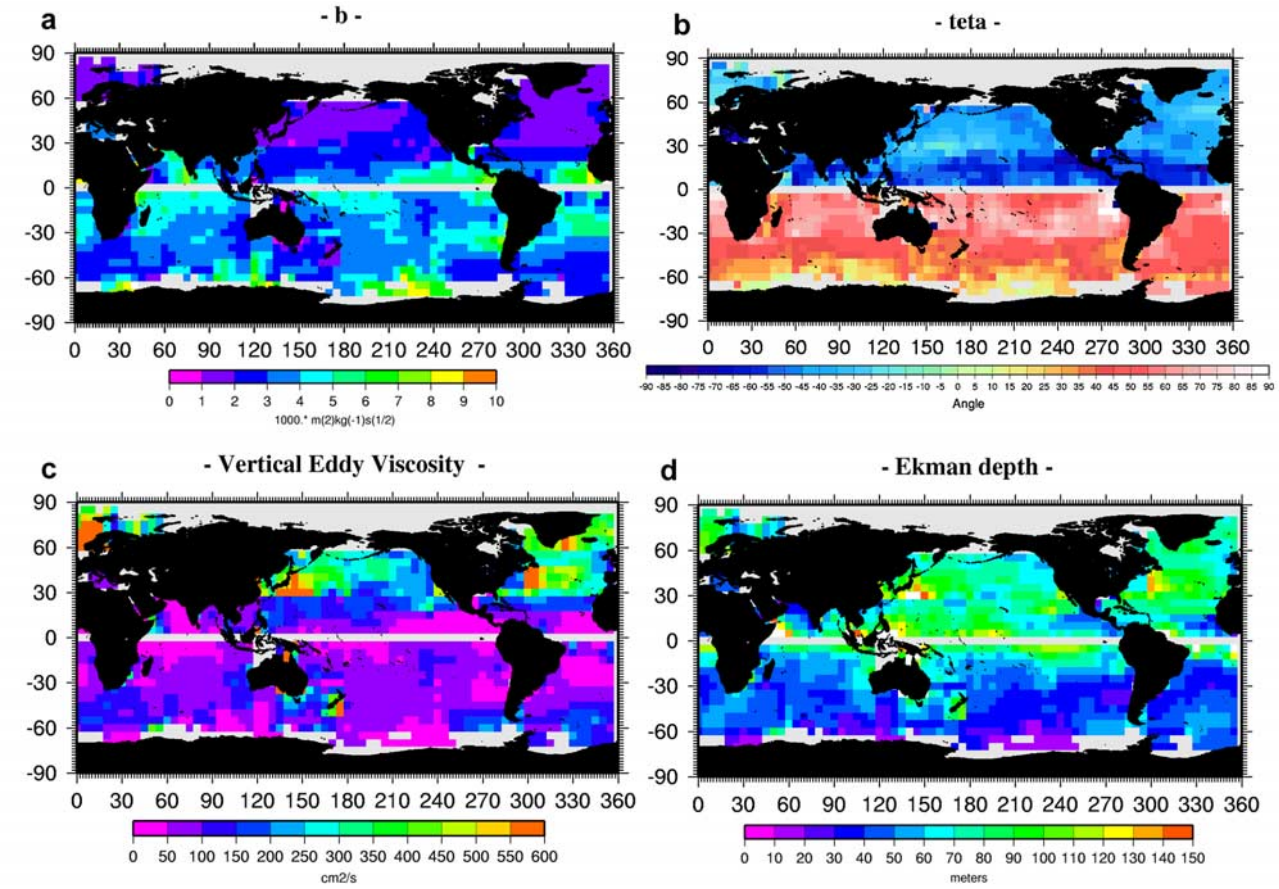

Figure 10. The *b* and θ parameters and the corresponding values of Ekman layer depth and vertical eddy viscosity for boreal winter (austral summer).

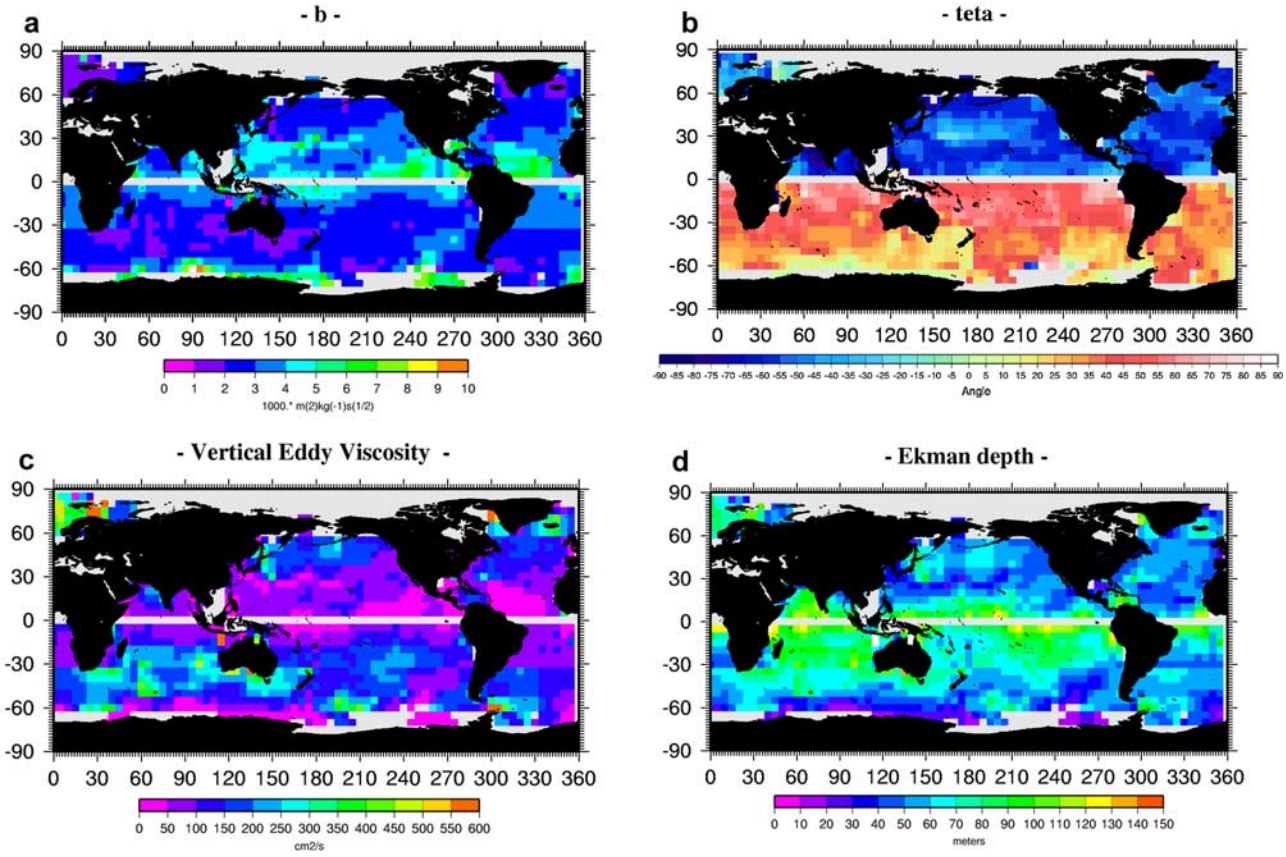

Figure 11. The b and θ parameters and the corresponding values of Ekman layer depth and vertical eddy viscosity for boreal summer (austral winter).

events, representing instead a *mean* behavior of the near-surface currents with respect to wind forcing.

6.3.2. Amplitude Parameter *b*

[59] We now analyze the seasonal variability of the b parameter by considering the associated values of the Ekman layer depth D_e and the viscosity ν. In winter, due to stronger winds, higher momentum is transmitted through friction throughout the mixed layer. This results in higher values of the Ekman layer depth and the eddy viscosity, as observed in Figures 10, 11, and 12.

6.3.3. Eddy Viscosity

[60] Eddy viscosity ranges from 250 to 600 cm^2/s during boreal winter and from 0 to 250 cm^2/s during boreal summer. Values are lower in the Southern Hemisphere, ranging from 150 to 300 cm^2/s during the austral winter and from 0 to 150 cm^2/s during the austral summer. However, in the equatorial band [−10°−10°], values are found to remain quite constant throughout the year, ranging from 0 to 150 cm^2/s.

[61] Typical eddy viscosity values found in the ocean vary from 0.1 to 1000 cm^2/s. In fact, various methods can be chosen to estimate the ocean eddy viscosity, leading to different results. *Santiago-Mandujano and Firing* [1990] reviewed eddy viscosity values computed in previous studies for the equatorial and tropical oceans ranging from 1 to 180 cm^2/s, depending on location and method. Several authors deduced eddy viscosity values from the observation of an Ekman like spiral [*Weller*, 1981; *Chereskin*, 1995; *Schudlich and Price*, 1998]. A difficulty arose as the observed spirals were in each case flatter than the theoretical Ekman spiral. Two different values of ν could therefore be estimated, based on amplitude decay or anticyclonic rate of rotation.

[62] In January 1977 along the coast of California, *Weller* [1981] found $\nu = 500$ cm^2/s using phase and $\nu = 50$ cm^2/s using amplitude. In that region, using winter data, we find $\nu = 450$ cm^2/s. In the California current, using data spanning from April to October 1993, *Chereskin* [1995] found $\nu = 1011$ cm^2/s using phase and $\nu = 274$ cm^2/s using amplitude. In that region, using summer data, we find a smaller value, $\nu = 88$ cm^2/s.

[63] In the Western Sargasso Sea, *Schudlich and Price* [1998] deduced in summer $\nu = 60$ cm^2/s based on amplitude decay and $\nu = 540$ cm^2/s based on phase decay. In winter, they found $\nu = 250$ cm^2/s based on amplitude decay and $\nu = 650$ cm^2/s based on phase decay. In that region we find $\nu = 100$ cm^2/s for summer and $\nu = 180$ cm^2/s for winter. We shall note that consequently to equation (3), uncertainties on ν are proportional to the square of uncertainties on b, so the viscosity values may be very sensitive to errors on b.

6.3.4. Ekman Layer Depth

[64] Ekman layer depth ranges from 60 to 120 m during boreal winter and from 30 to 60 m during boreal summer. Values of the same order are obtained in the Southern Hemisphere, except in the subpolar latitudes where smaller values are observed in winter (0–50 m). As for the eddy

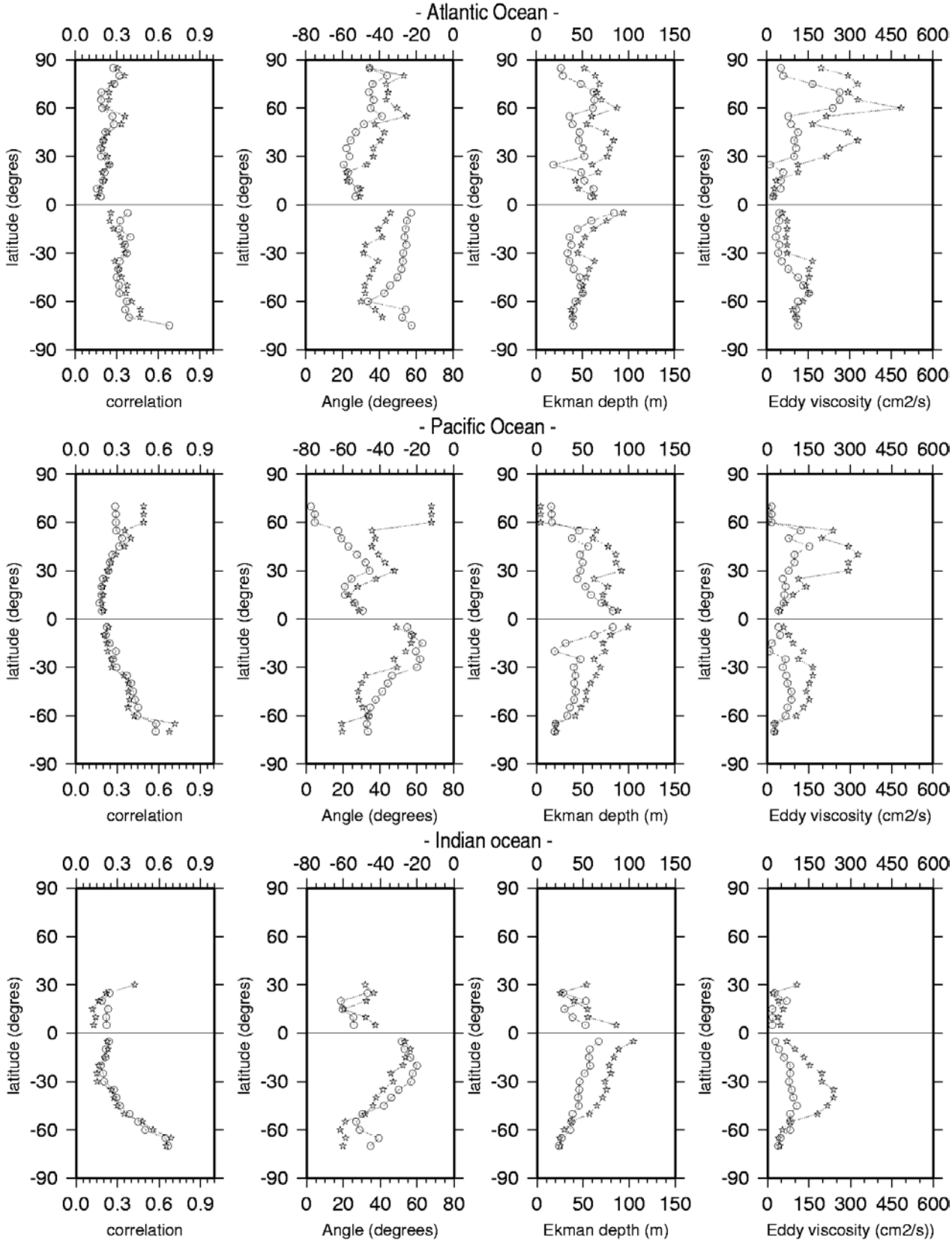

Figure 12. Mean longitudinal values for summer (circles) and winter (stars).

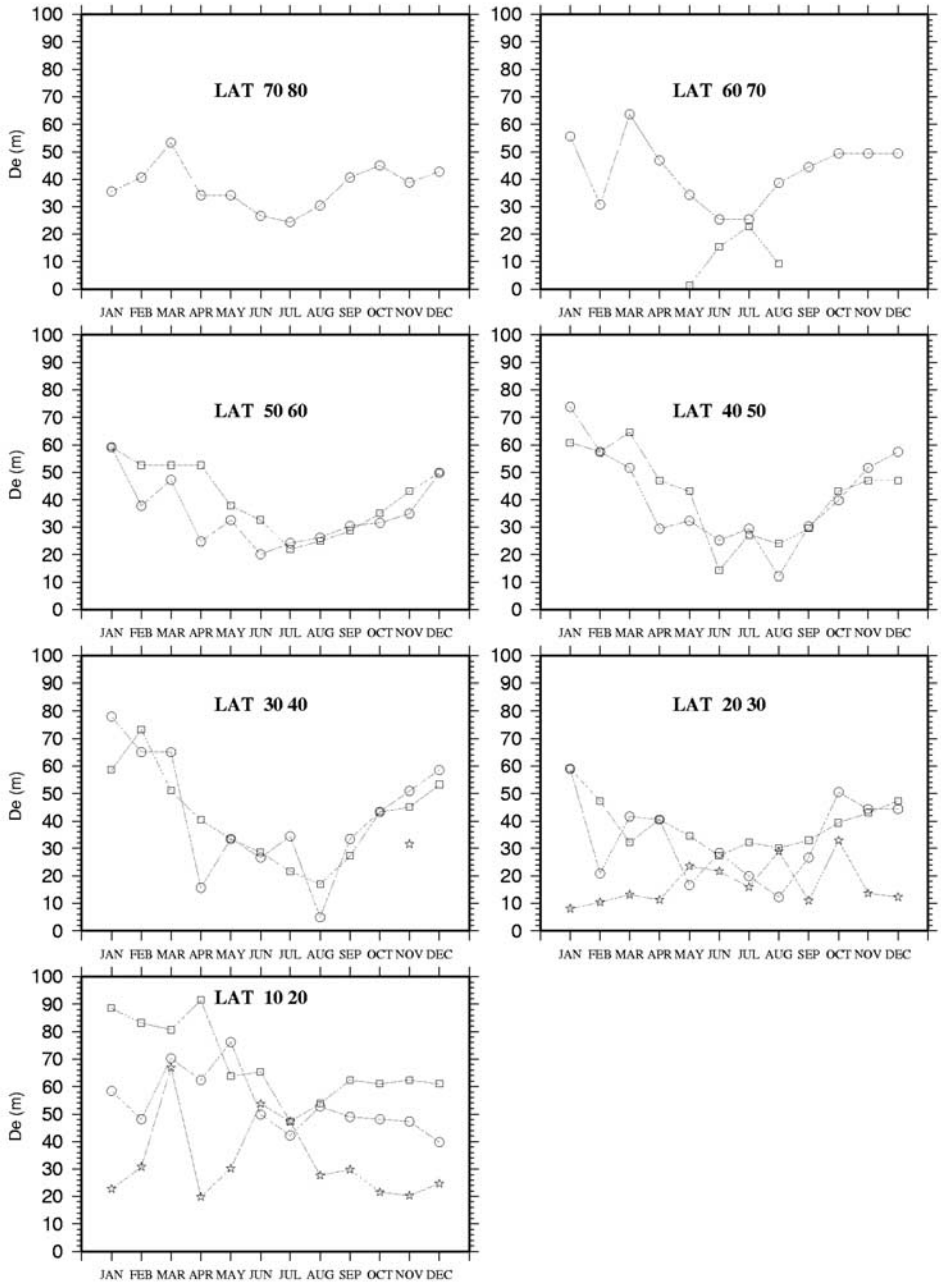

Figure 13. Monthly mean Ekman depth values for the Atlantic ocean (circles), the Pacific Ocean (squares), and the Indian Ocean (stars) in the Northern Hemisphere.

viscosity, values in the equatorial band [−10:10] range between 60 and 120 m throughout the year.

6.3.4.1. Comparisons With Other Studies

[65] *Chereskin* [1995] found in the California current from April to October 1993 an e-folding depth D_e = 25 m, based on amplitude decay, and D_e = 48 meters based on phase rotation. We find in this region, based on summer observations, D_e = 44 m (Figure 11).

[66] *Niiler and Paduan* [1995] found in the northeast Pacific during fall 1987 and winter 1989–1990 a mixing depth H = 34–38 m corresponding to an e-folding depth D_e = 48–54 m. Using the same data, *Meurs and Niiler* [1997] found a mixing depth H = 33 m corresponding to an e-folding depth D_e = 47 m. In this region, using the winter observations, we find D_e ranging from 40 to 50 m.

[67] In the tropical pacific, *Lagerloef et al.* [1999] and *Ralph and Niiler* [1999] found e-folding depth D_e = 37 m and D_e = 46 m, respectively. We find higher values for that region (40 m < D_e < 90 m).

6.3.4.2. Seasonal Cycle

[68] To investigate further the seasonal variability of the Ekman layer depth, we now compute monthly values (averaged zonally) for each 10° latitude band. Results are presented Figure 13 for the Northern Hemisphere and

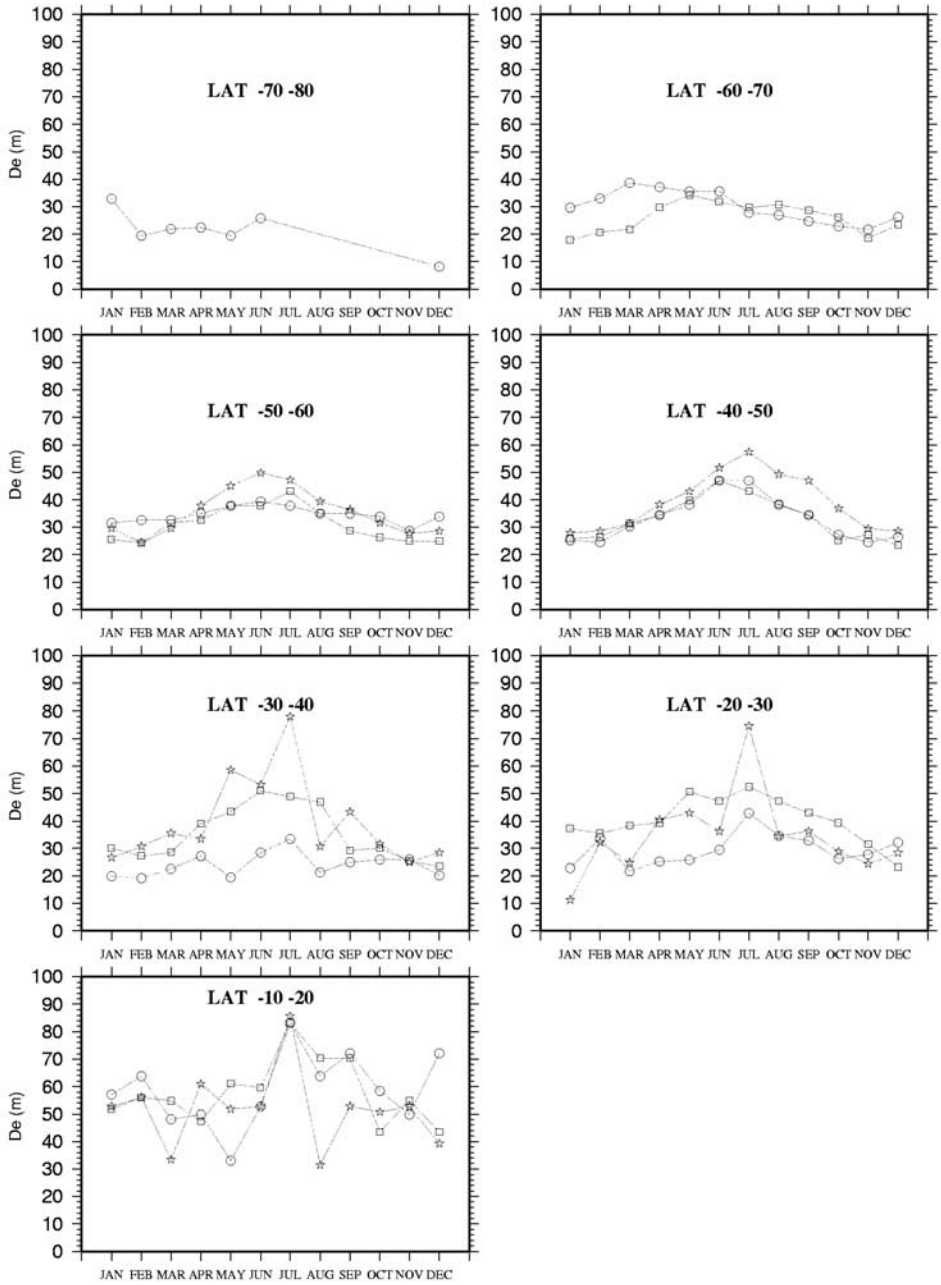

Figure 14. Monthly mean Ekman depth values for the Atlantic ocean (circles), the Pacific Ocean (squares), and the Indian Ocean (stars) in the Southern Hemisphere.

Figure 14 for the Southern Hemisphere. This is possible thanks to the high amount of data available for this study. As a result, the monthly results are statistically significant, at least at low and middle latitudes.

[69] Except for the northern Indian Ocean, where the monsoon wind regime is very specific, a very clear seasonal cycle is observed from 60°S to 80°N. The cycle is less pronounced at latitudes poleward of 60°S, (where fewer data are available) and at latitudes between −20° and 20° (where the wind stress seasonal cycle is weaker).

[70] The Indian Ocean exhibits larger Ekman layer depth values than the other oceans at all latitudes, with a maximum of 80 m in July for latitudes between −20° and −40° and 50–60 m for the other latitudes. The Pacific Ocean exhibits larger values than the Atlantic Ocean in the latitude range [−40°; −20°] with maximum values close to 50 m (30–40 m for the Atlantic Ocean) and minimum values of 30–40 m (20 m for the Atlantic Ocean). At latitudes ranging from −40° to −50°, the seasonal cycle is similar for both oceans with a minimum value of 25 m and a maximum value of 45 m.

[71] In the Northern Hemisphere, the Ekman layer depth is minimal in July and August (values equal to 10–30 m), increases regularly until January–February–March (maxi-

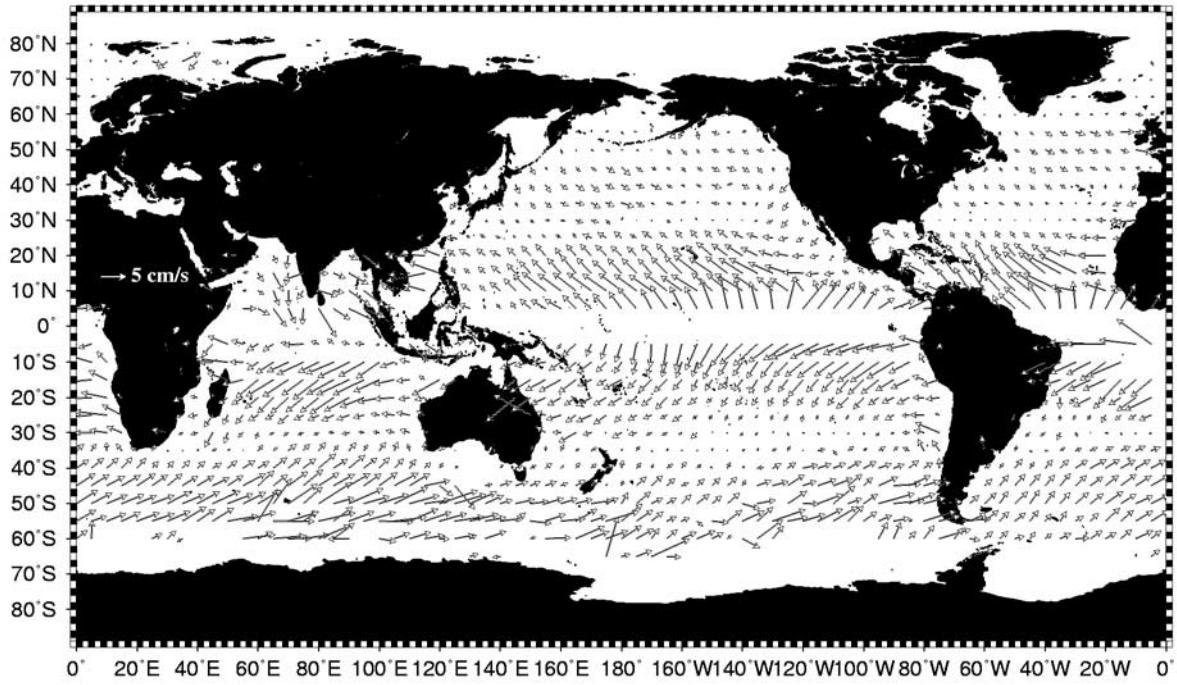

Figure 15. Mean wind-driven velocities in 5° × 5° boxes.

mum values between 60 and 80 m), and then decreases again regularly until July–August. The Pacific and Atlantic Ocean follow quite the same cycle, although Pacific values are slightly higher in spring for latitudes between 40° and 60°. Besides, the amplitude of the annual cycle observed in the Atlantic is higher than in the Pacific.

[72] In the Southern Hemisphere, an opposite cycle is observed with minimum values obtained between January and March and maximum values obtained between June and August. For each latitudinal band, we also computed the seasonal cycles of the wind stress data and of the sea surface temperature (SST) data from the Levitus climatology [*Levitus and Boyer*, 1994]. The minimum/maximum observed in the Ekman layer depth cycles correspond rather to the atmospheric seasonal minimum/maximum (December/July) than to the SST maximum/minimum (February/September). Owing to the oceanic adjustment, the minimum and maximum in the SST cycle occurs one to three months later than in the atmospheric seasonal cycle. The Ekman layer depth computed in our study corresponds to the fast response of the ocean to atmospheric forcing.

7. Mean Ageostrophic Velocity Field

[73] We now use the b and θ parameters obtained in section VI to compute Ekman current velocities for the global ocean. At each drifter's position where we interpolated a wind stress value, we compute the corresponding Ekman velocity,

$$\vec{u}_e = \frac{b\,\vec{\tau}}{\sqrt{f}} e^{i\theta}.$$

We use the b and θ winter (summer) results for drifting buoy positions recorded in winter (summer).

[74] Mean values (Figure 15) and variances (Figure 16) in the years 1993–1999 were computed on a 5° grid. The general pattern features a strong divergence slightly south of the equator with meridional velocities reaching 5–7 cm/s in the central Pacific, just north of the equator, and −2 to −4 cm/s just south of the equator. A clear convergence is observed at 30°N and 30°S in all oceans with meridional velocities of 1–3 cm/s. In the southern oceans, south of −30°, strong Ekman current velocities are obtained, the zonal component reaching 3–6 cm/s and the meridian component reaching 2–4 cm/s.

[75] This corresponds to the classical low-frequency current response to the global wind system: Easterly winds at the equator lead to the so-called equatorial divergence; at 30°N a convergence is observed between the northeast trades (wind-driven layer moving to the northwest) and the westerlies (wind-driven layer moving to the south). Similarly, at 30°S the convergence is between the southeast trades (wind-driven layer moving to the southwest) and the westerlies (wind-driven layer moving to the north).

[76] The highest variability is obtained for the zonal component north of 30°S (values ranging from 4 to 7 cm/s compared to 0 to 4 cm/s for the meridional component). South of 30°S the variance is more isotropic, with values ranging between 4 and 7 cm/s.

8. Summary and Conclusions

[77] Extracting the wind-driven current response from the total oceanographic signal given by in situ current measurements has always been a key problem for checking the Ekman theory in the open ocean. Incorporating altimetric data has rarely been investigated [*Lagerloef et al.*, 1999]. This method achieves a better separation of the geostrophic

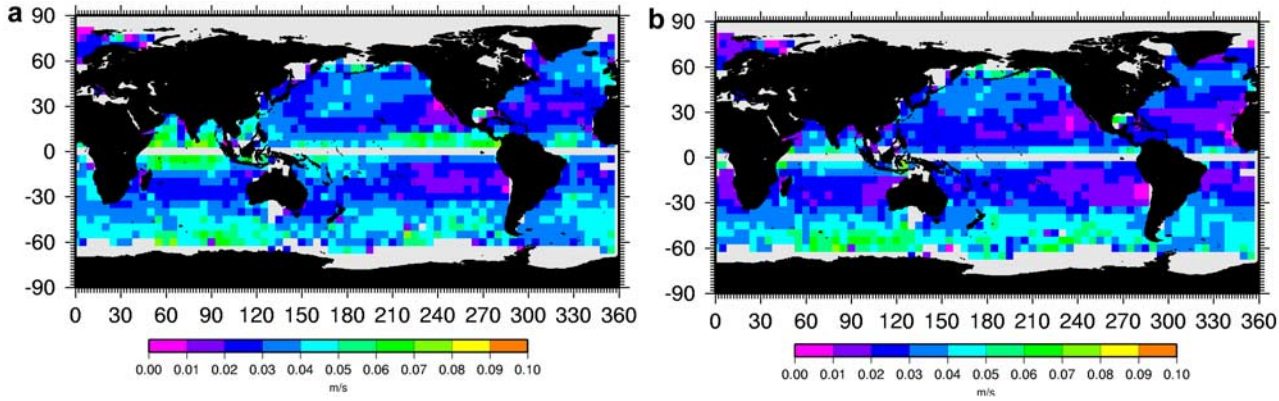

Figure 16. (a) Zonal and (b) meridional wind-driven velocitiy variance in 5° × 5° boxes.

component from the drifter velocities so that the residual velocity can be considered as mainly directly wind-driven.

[78] The high spatial and temporal altimetry coverage and the large amount of drifter data gathered between 1993 and 1999 as part of the WOCE Surface Velocity Program are used to make the first global, homogeneous, and statistically meaningful inventory of the high-frequency wind-driven current response in the upper layers of the ocean, and of its seasonal variability. The study describes the global near-surface current response to wind stress forcing at high frequency (i.e., for periods between the inertial period and 20 days). Wind stress, drifter velocities, and altimetry surface heights were considered for the years spanning 1993 to 1999, with global coverage.

[79] The ageostrophic drifter velocity components were obtained by removing altimetry deduced geostrophic velocities. Spectral analysis underlined the energetic part of the total velocity signal contained in the geostrophic velocity component. This part represents up to half of the total signal for periods longer than 10 days in the [15°–30°] latitude band and longer than 4 days in the [30°–90°] latitude band. Thus, for those periods, the vector cross-spectral analysis applied to wind stress and drifter velocities resulted in higher coherence when only the ageostrophic component of the near-surface current velocity is considered. The phase between the two vectors was found to be consistent with theory [*Gonella*, 1972]. Low coherence combined with highly scattered angle distribution were obtained at sub-inertial periods, where the wind-driven current is contaminated by phenomena like tidal and inertial oscillations and by wind stress errors. Also, high-frequency results have to take into account that aliasing can be present in the 6-hourly ECMWF wind products and also in the kriged velocity buoy data set. These phenomena were removed using a low-pass filter. For sub-20-day superinertial periods, we considered the ageostrophic drifter velocities to model the near-surface, high-frequency wind-driven currents.

[80] A two-parameter (i.e., amplitude and angle) model was then fitted to the wind stress and the estimated wind-driven velocity data using a least squares method. The angle parameter describes the wind-driven currents to be directed to the right (left) of the wind stress direction in the Northern (Southern) Hemisphere, with an angle ranging from 40° to 70° at latitudes equatorward of 30° and from 10° to 40° poleward of 30°. This latitudinal variability is explained by higher stratification in the upper ocean at low latitudes. Looking at the seasonal cycle, we find that the angle increases by 10°–20° in the summer compared to winter, coherent with the higher summer stratification.

[81] For more physical relevance in studying the amplitude parameter, we derive from b the Ekman layer depth (e-folding depth) D_e and the vertical eddy viscosity value ν. Both these terms are higher in winter than in summer. Discrepancies with other studies are due to applied model and data differences. Besides, we consider data spanning 7 years, so the effects of wind stress interannual variability present in other studies are removed.

[82] Monthly values of D_e were computed for all oceans in 10° latitude bands. A clear seasonal cycle between 20° and 60° (north and south) was observed with a minimum (maximum) value obtained between June and August and a maximum (minimum) value obtained in January–March for the Northern (Southern) Hemisphere. This observed seasonal cycle corresponds to the atmospheric cycle rather than to the ocean sea surface temperature cycle. Seasonal amplitudes of D_e ranging from 10 to 20 m are obtained in the Southern Hemisphere, with the exception of the Indian Ocean where the maximum amplitude obtained is 70 m (between [−20;−30]). In the Northern Hemisphere, amplitudes of 40–70 m are obtained for the Pacific and Atlantic Oceans.

[83] Finally, we used the parameters obtained globally to compute wind-driven currents at a depth of 15 m from the wind stress data. These velocities were averaged into 5° boxes. The low-frequency response of the upper ocean to wind stress is present in this data set, with a strong equatorial divergence and convergences at 30°N and 30°S.

[84] Our modeling effort has clearly identified an Ekman-like response over the entire globe, in spite of the low variance explained. Our method depends on the quality of the data sets used to represent the wind-driven currents and the wind stress field. Results should be improved in the future with the systematic use of satellite-borne scatterometer measurements to compute wind stress fields on smaller spatial and temporal scales.

References

Atlas, R., R. Hoffman, S. Bloom, J. Jusem, and J. Ardizzone, A multiyear global surface wind velocity dataset using SSM/I wind observations, *Bull. Am. Meteorol. Soc.*, *77*, 869–882, 1996.

Chereskin, T. K., Direct evidence for an Ekman balance in the California Current, *J. Geophys. Res.*, *100*, 18,261–18,269, 1995.

Chereskin, T. K., and D. Roemmich, A comparison of measured and wind-derived Ekman transport at 11°N in the Atlantic Ocean, *J. Phys. Oceanogr.*, *21*, 869–878, 1991.

Daniault, N., P. Blouch, and F.-X. Fusey, The use of free drifting meteorological buoys to study winds and surface currents, *Deep Sea Res.*, *32*, 107–113, 1985.

Davis, R. E., R. DeSzoeke, and P. Niiler, Variability in the upper ocean during MILE: II. Modeling the mixed layer response, *Deep Sea Res., Part A*, *28*, 1453–1475, 1981.

Ekman, V. W., On the influence of the Earth's rotation on ocean currents, *Ark. Mat. Aston. Fys.*, *2*(11), 1–53, 1905.

Glenn, S. M., D. L. Porter, and A. R. Robinson, A Synthetic geoid validation of Geosat mesoscale dynamic topography in the Gulf Stream region, *J. Geophys. Res.*, *96*, 7145–7166, 1991.

Gonella, J., A rotary component method for analysing meteorological and oceanographic vector time series, *Deep. Sea. Res.*, *19*, 833–846, 1972.

Hansen, D. V., and P.-M. Poulain, Quality control and interpolation of WOCE/TOGA drifter data, *J. Atmos. Oceanic Technol.*, *13*, 900–909, 1996.

Hernandez, F., Comparaison et combinaison de données altimétriques et lagrangiennes: Application à la campagne SEMAPHORE-93, *UMR39/GRGS/OMP*, 276 pp., Univ. Paul Sabatier (Toulouse III), Toulouse, France, 1995.

Hernandez, F., P.-Y. Le Traon, and R. Morrow, Mapping mesoscale variability of the Azores Current using TOPEX/POSEIDON and ERS-1 altimetry, together with hydrographic and Lagrangian measurements, *J. Geophys. Res.*, *100*, 24,995–25,006, 1995.

Kalos, M. H., and P. A. Whitlock, *Monte Carlo Methods*, vol. 1, *Basics*, John Wiley, New York, 1986.

Lagerloef, G. S. E., G. T. Mitchum, R. B. Lukas, and P. P. Niiler, Tropical Pacific near-surface currents estimated from altimeter, wind, and drifter data, *J. Geophys. Res.*, *104*, 23,313–23,326, 1999.

Lee, C. M., The subinertial momentum balance of the North Atlantic Subtropical Convergence Zone, *J. Phys. Oceanogr.*, *26*, 1690–1704, 1996.

Le Traon, P. Y., and G. Dibarboure, Velocity mapping capabilities of present and future altimeter missions: The role of high frequency signals, *J. Atmos. Oceanic Technol.*, *19*, 2077–2088, 2002.

Le Traon, P.-Y., F. Nadal, and N. Ducet, An improved mapping method of multisatellite altimeter data, *J. Atmos. Oceanic Technol.*, *15*, 522–534, 1998.

Levitus, S., Climatological atlas of the world ocean, *Prof. Pap. 13*, 173 pp., Natl. Ocean and Atmos. Admin., Silver Spring, Md., 1982.

Levitus, S., and T. P. Boyer, *World Ocean Atlas 1994*, vol. 4, *Temperature*, *NOAA Atlas NESDIS 4*, 117 pp., Natl. Ocean and Atmos. Admin., Silver Spring, Md., 1994.

McNally, G. J., D. S. Luther, and W. B. White, Subinertial frequency response of wind-driven currents in the mixed layer measured by drifting buoys in the midlatitude North Pacific, *J. Phys. Oceanogr.*, *19*, 290–300, 1989.

Meurs, P. V., and P. P. Niiler, Temporal variability of the large-scale geostrophic surface velocity in the Northeast Pacific, *J. Phys. Oceanogr.*, *27*, 2288–2297, 1997.

Mitchell, J. L., J. M. Dastugue, W. J. Teague, and Z. R. Hallock, Estimation of geoid profiles in the northwest Atlantic from simultaneous satellite altimetry and airborne expendable bathythermograph sections, *J. Geophys. Res.*, *95*, 17,965–17,977, 1990.

Mooers, C. N. K., The interaction of an internal tide with the frontal zone in a coastal upwelling region, Ph.D. thesis, 480 pp., Oregon State Univ., Corvallis, Oreg., 1970.

Mooers, C. N. K., A technique for the cross spectrum analysis of pairs of complex-valued time series, with emphasis on properties of polarized components and rotational invariants, *Deep Sea Res.*, *20*, 1129–1141, 1973.

Niiler, P. P., and J. D. Paduan, Wind-driven motions in the northeast Pacific as measured by Lagrangian drifters, *J. Phys. Oceanogr.*, *25*, 2819–2830, 1995.

Niiler, P. P., R. E. Davis, and H. J. White, Water-following characteristics of a mixed layer drifter, *Deep Sea Res., Part I*, *34*, 1867–1881, 1987.

Niiler, P. P., A. S. Sybrandy, K. Bi, P.-M. Poulain, and D. Bitterman, Measurements of the water-following characteristics of Tristar and Holey-sock drifters, *Deep Sea Res.*, *42*, 1951–1964, 1995.

Pollard, R. T., and J. R. C. Millard, Comparison between observed and simulated wind-generated inertial oscillations, *Deep Sea Res.*, *17*, 813–821, 1970.

Poulain, P.-M., Near-inertial and diurnal motions in the trajectories of mixed-layer drifters, *J. Mar. Res.*, *48*, 793–823, 1990.

Price, J. F., and R. A. Weller, Diurnal cycling: Observations and models of the upper ocean response to diurnal heating, cooling and mixing, *J. Geophys. Res.*, *91*, 8411–8427, 1986.

Price, J. F., R. A. Weller, and R. R. Schudlich, Wind-driven ocean currents and Ekman transport, *Science*, *238*, 1534–1538, 1987.

Ralph, E. A., and P. P. Niiler, Wind-driven currents in the tropical Pacific, *J. Phys. Oceanogr.*, *29*, 2121–2129, 1999.

Rio, M.-H., and F. Hernandez, Estimation of a mean dynamic topography for the North and tropical Atlantic, report, 48 pp., CLS, Ramonville-St. Agne, France, 2002.

Rudnick, D. L., and R. A. Weller, Observations of superinertial and near-inertial wind-driven flow, *J. Phys. Oceanogr.*, *23*, 2351–2359, 1993.

Santiago-Mandujano, F., and E. Firing, Mixed-layer shear generated by wind stress in the central equatorial Pacific, *J. Phys. Oceanogr.*, *20*, 1576–1582, 1990.

Schudlich, R. R., and J. F. Price, Observations of seasonal variation in the Ekman layer, *J. Phys. Oceanogr.*, *28*, 1187–1204, 1998.

Vialar, J., Calcul des probabilités et statistiques: Statistiques, contingences et correlations, *Cours Minist. Transports Tome 3*, Secr. Gén. de l'Aviation Civ., Direction de la Météorologie, Casablanca, Morocco, 1978.

Weller, R. A., Observations of the velocity response to wind forcing in the upper ocean, *J. Geophys. Res.*, *86*, 1969–1977, 1981.

Weller, R. A., and A. J. Plueddemann, Observations of the vertical structure of the oceanic boundary layer, *J. Geophys. Res.*, *101*, 8789–8806, 1996.

Weller, R. A., D. L. Rudnick, C. C. Eriksen, K. L. Polzin, N. S. Oakey, J. W. Toole, R. W. Schmitt, and R. T. Pollard, The forced ocean response during the Frontal Air-Sea Interaction Experiment, *J. Geophys. Res.*, *96*, 8611–8638, 1991.

Wijffels, S., E. Firing, and H. Bryden, Direct observations of the Ekman balance at 10°N in the Pacific, *J. Phys. Oceanogr.*, *24*, 1666–1679, 1994.

F. Hernandez, CLS, Space Oceanography Division, 8-10 Rue Hermes, Parc Technologique du Canal, 31526 Ramonville Saint-Agne, France. (Fabrice.Hernandez@cls.fr)

M.-H. Rio, Istituto di Scienze dell'Atmosfera e del Clima-CNR, Via Fosso del Cavaliere 100, 00133 Roma, Italy. (MH.rio@isac.cnr.it)